

## NORTH – SOUTH ASYMMETRY OF ZONAL AND MERIDIONAL FLOWS DETERMINED FROM RING DIAGRAM ANALYSIS OF GONG++ DATA

A. ZAATRI

*Centre de Recherche en Astronomie Astrophysique et Geophysique, B.P. 63 Bouzaréah, Algiers  
16340, Algeria*

R. KOMM, I. GONZÁLEZ HERNÁNDEZ, and R. HOWE

*National Solar Observatory, 950 N. Cherry Ave., Tucson, AZ 85719, U.S.A.  
(e-mail: rkomm@nso.edu)*

and

T. CORBARD

*Observatoire de la Côte d'Azur, F-06304 Nice Cedex 4, France*

(Received 17 November 2005; accepted 28 March 2006)

**Abstract.** We study the North – South asymmetry of zonal and meridional components of horizontal, solar subsurface flows during the years 2001 – 2004, which cover the declining phase of solar cycle 23. We measure the horizontal flows from the near-surface layers to 16 Mm depth by analyzing 44 consecutive Carrington rotations of Global Oscillation Network Group (GONG) Doppler images with a ring-diagram analysis technique. The meridional flow and the errors of both flow components show an annual variation related to the  $B_0$ -angle variation, while the zonal flow is less affected by the  $B_0$ -angle variation. After correcting for this effect, the meridional flow is mainly poleward but it shows a counter cell close to the surface at high latitudes in both hemispheres. During the declining phase of the solar cycle, the meridional flow mainly increases with time at latitudes poleward of about  $20^\circ$ , while it mainly decreases at more equatorward latitudes. The temporal variation of the zonal flow in both hemispheres is significantly correlated at latitudes less than about  $20^\circ$ . The zonal flow is larger in the southern hemisphere than the northern one, and this North – South asymmetry increases with depth. Details of the North – South asymmetry of zonal and meridional flow reflect the North – South asymmetry of the magnetic flux. The North – South asymmetries of the flows show hints of a variation with the solar cycle.

### 1. Introduction

We study the zonal and meridional flow in shallow solar subsurface layers: their temporal variability and North – South asymmetry during the declining phase of the solar cycle. For this purpose, we analyze 44 consecutive Carrington rotations of Global Oscillation Network Group (GONG) Doppler images using the GONG ring-diagram analysis pipeline.

Large-scale zonal and meridional flows play an important role in solar dynamo theory (*e.g.*, Charbonneau, 2005). For example, the transport of magnetic flux by the meridional flow is a key ingredient in some dynamo models (Dikpati and Gilman,

2001; Nandy and Choudhuri, 2002). The North–South asymmetry of the meridional flow can cause the polar field in one hemisphere to reverse before the polar field in the other (Dikpati *et al.*, 2004).

Long-term meridional and zonal-flow variability in subsurface layers have been studied using different methods of local helioseismology and different data sets. Zhao and Kosovichev (2004) analyzed Michelson Doppler Imager (MDI) Dynamics Program data with the time-distance method to study the solar-cycle variation of the zonal flow, the so-called torsional oscillation pattern, and the variation of the meridional flow. Haber *et al.* (2002) studied the long-term variation of the zonal and the meridional flow applying the ring-diagram technique to MDI Dynamics Program data. Chou and Dai (2001) and Chou and Ladenkov (2005) applied the time-distance technique to Taiwan Oscillation Network (TON) data to study the meridional flow during the rising and declining phase of the solar cycle. In addition to an essentially-poleward meridional flow, these studies find that the meridional flow converges toward the mean latitude of magnetic activity at depths less than about ten Mm and that it diverges at greater depth. Chou and Ladenkov (2005) find that the amplitude of the divergent flow increases with depth to about 90% of the solar radius and then decreases with depth at least down to about 80% of the radius. Basu and Antia (2003) found changes related to solar activity in the North–South asymmetries of horizontal flows derived from nine Carrington rotations of MDI data covering the rising phase of solar cycle 23. In particular, the antisymmetric component of the meridional flow decreases in amplitude with increasing activity.

The goal of this paper is to study the zonal and meridional flow variability during the declining phase of the solar cycle 23 from mid-2001 to end-2004 with a standard ring-diagram analysis of high-resolution GONG data. However, this is a rather “boring” epoch as far as large-scale flows are concerned since the mean latitude of magnetic activity (about  $15^\circ$ ) changes little during this time, moving somewhat toward the equator.

Given the length of the data set and the rather constant distribution of magnetic activity, we can check the derived flows for systematic variations of observational origin that might bias the results. As part of the ring-diagram analysis, effects such as the variation throughout the year of the solar inclination toward the Earth, the  $B_0$ -angle, are taken into account. But, the processing cannot correct for a loss in detail that can occur at high spatial frequencies due to this variation. For example, González Hernández *et al.* (2006) found in a large-aperture ring-diagram analysis of high-resolution GONG data that an equatorward meridional cell appears at high latitudes during maximum values of the  $B_0$ -angle and that it appears either in the northern or southern hemisphere depending on the sign of the  $B_0$ -angle. Finally, we correct the measured horizontal flows for these systematic effects and focus on their temporal variations and North–South asymmetry.

## 2. Data Analysis

The data used in this work consist of continuous, high-resolution Dopplergrams from the Global Oscillation Network Group (GONG) covering 44 consecutive Carrington rotations from CR 1979 to CR 2022 (July 27, 2001 – October 12, 2004). Full-disk Dopplergrams at one minute cadence are recorded on a  $1024 \times 1024$  pixel CCD (Harvey, Tucker, and Britanik, 1998) and then registered so that the solar image covers an area of 800 pixels in diameter (GONG++ data). In order to measure the horizontal components of the solar subsurface flows as a function of depth, we use one of the local helioseismology techniques called ring-diagram analysis (Hill, 1988; Morrow, 1988). This technique uses high-degree acoustic waves measured in small patches in the plane-wave approximation. This simplification is good enough for studying subsurface layers close to the surface. The wave pattern is advected by a local velocity field and the resulting shift of the wave pattern can be used to determine the subsurface flows (Gough and Toomre, 1983).

We use the dense-pack technique as described by Haber *et al.* (2002) for their analysis of Michelson Doppler Imager (MDI) Dynamics Program data. For GONG++ data, simultaneous images from different sites are merged (Toner *et al.*, 2003), and the time series of merged images is analyzed in “days” of 1664 minutes duration. For each day, the merged full-disk Dopplergrams are remapped into a set of 189 overlapping patches with centers separated by  $7.5^\circ$  in latitude and longitude covering the solar disk from the central meridian to  $\pm 52.5^\circ$  in longitude and  $\pm 52.5^\circ$  in latitude. Each patch of  $16^\circ \times 16^\circ$  diameter is tracked at the surface rotation rate (Snodgrass, 1984) in order to remove the differential rotation effect and apodized with a circular function reducing the effective diameter to  $15^\circ$ . Three-dimensional power spectra are constructed from each dense-pack patch using a three-dimensional FFT so that each data cube in spatial and temporal coordinates  $(x, y, t)$  is transformed into one described in horizontal wavenumbers  $(k_x, k_y)$  and temporal frequency  $(\nu)$ . Two-dimensional slices of the power spectra at a specified temporal frequency show “rings” which are shifted in  $k_x, k_y$  by a velocity field. The power spectrum is then fitted with a Lorentzian profile model which incorporates a perturbation term  $(k_x v_x + k_y v_y)$  due to the horizontal velocity components. Finally, the Regularized Least Square (RLS) method is used to invert the fitted velocities (Thompson *et al.*, 1996; Haber *et al.*, 2002) in order to derive the horizontal velocity components as functions of depth  $(v_x(r), v_y(r))$  for the East–West, or zonal, component and the North–South, or meridional, component. The analysis is described in more detail by Corbard *et al.* (2003) and implemented as the GONG ring-diagram pipeline as described by Hill *et al.* (2003).

In this way, we derive 189 pairs of zonal and meridional velocity at 16 depths from 0.6 to 16 Mm for each 1664-minute day. We combine these daily flow maps to calculate synoptic flow maps for each depth using a weighting factor of cosine central meridian distance to the fourth power. For this work, we average the horizontal flows over the length of a Carrington rotation and study the temporal variation of

zonal and meridional flows from more than three years of consecutive GONG++ data.

During the remapping stage, a variety of geometric effects are taken into account that vary with a period of one year, such as the solar inclination toward the Earth ( $B_0$ -angle) and the apparent semi-diameter of the Sun. However, the processing cannot correct for a loss in spatial resolution introduced by these effects. For example, a large  $B_0$ -angle value means that one solar hemisphere is tilted away from the observer which will increase the geometric foreshortening at a given solar latitude on this hemisphere. In order to check for annual variations introduced by these effects, we calculate the  $B_0$ -angle and the apparent semi-diameter for the middle of every Carrington rotation and compare their temporal variation with the variation of the measured zonal and meridional flows. The sidereal-synodic correction is a geometric effect (*e.g.*, Wittmann *et al.*, 1996) that influences the determination of the central meridian distance and can be expressed as a change in the tracking rate (Corbard *et al.*, 2003). While the average value of the sidereal-synodic correction is taken into account at the remapping stage, we calculate its value<sup>1</sup> for the middle of each Carrington rotation and correct the zonal flows for the annual variation of the sidereal-synodic correction.

As a measure of solar activity, we use the NSO Kitt Peak synoptic charts.<sup>2</sup> We rebin the magnetogram data into circular areas with  $15^\circ$  diameter centered on a grid with  $7.5^\circ$  spacing in latitude and longitude to match the dense-pack mosaic.

### 3. Results

#### 3.1. TEMPORAL VARIATION

Figure 1 shows the temporal variation of the meridional flow in the northern and southern hemisphere at four latitudes and four depths. The meridional flows are mainly poleward in each hemisphere, except at high latitudes and very close to the surface as indicated by the predominantly positive values of the southern flow and the negative values of the northern flow in the first panel ( $\pm 52.5^\circ$  and  $0.6$  Mm). These values indicate an equatorward flow, a so-called counter cell, close to the surface at high latitudes in both hemispheres.

At high latitudes and low depths, these meridional flows exhibit periodic trends recurring on a yearly basis. For comparison, we include the variation of the  $B_0$ -angle with time. The  $B_0$ -angle has an annual periodicity, and its variation seems to be well correlated with that of the meridional flows in these regions. In order to better visualize this correlation, we include a linear regression of the flow with the  $B_0$ -angle on the same chart. Furthermore, correlation coefficients, shown in Figure 2 at the same latitudes and depths, show overall a good correlation between the  $B_0$ -angle

<sup>1</sup>see <http://aa.usno.navy.mil/faq/docs/SunApprox.html>

<sup>2</sup>Available at <http://nsokp.nso.edu/dataarch.html>

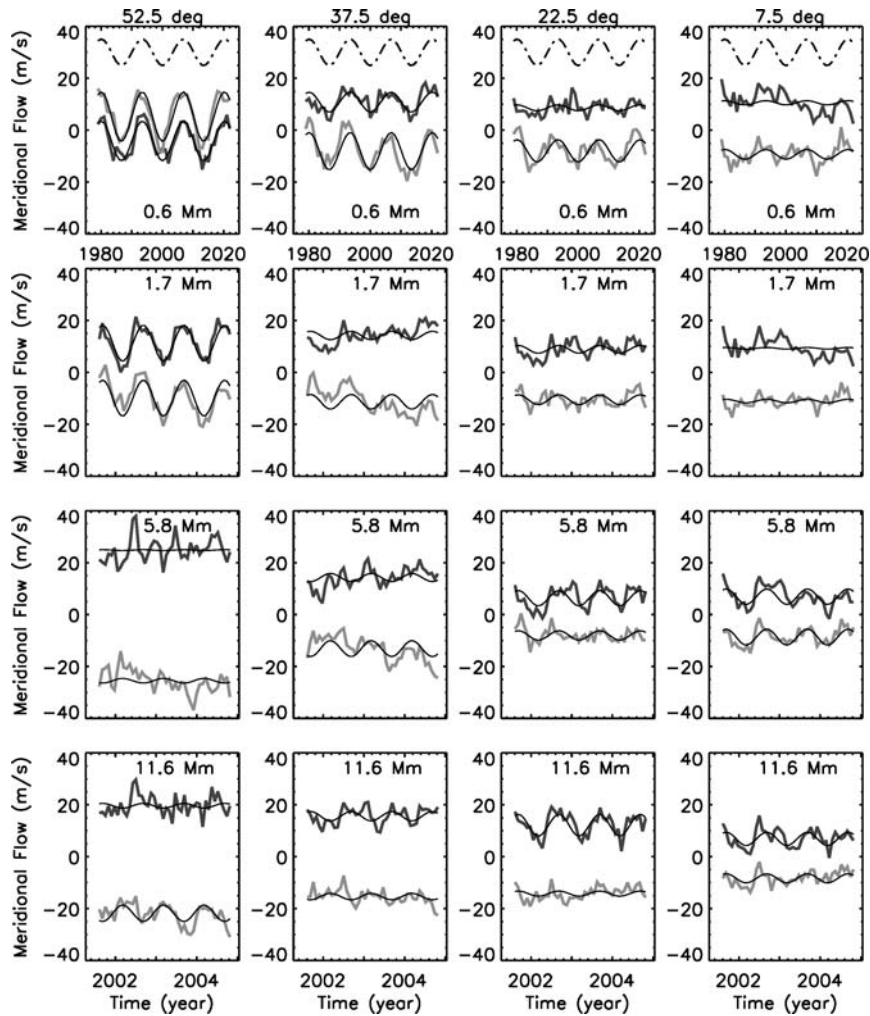


Figure 1. Temporal variation of the meridional flow in the northern (*dark grey*) and southern hemisphere (*light grey*) at four latitudes and four depths. The *line thickness* represents about two standard deviations of the formal uncertainty. Positive (negative) values indicate flows to the North (South). The top row shows, for comparison, the time scale in Carrington Rotations. The  $B_0$ -angle variation (in degree) is indicated as dot-dashed line in the top row (shifted by 30 m/s in the y direction). *Thin solid lines* represent linear fits of the  $B_0$ -angle to the flows.

and flow variabilities. Large correlation coefficients occur mainly at high latitudes, while the values are generally small close to the equator. The correlation values are very similar in both hemispheres except at shallow layers equatorward of about  $30^\circ$  and at depths greater than about ten Mm poleward of about  $30^\circ$ .

For comparison, we also calculate the correlation between the meridional flow and the apparent semi-diameter, which varies with an annual period but about

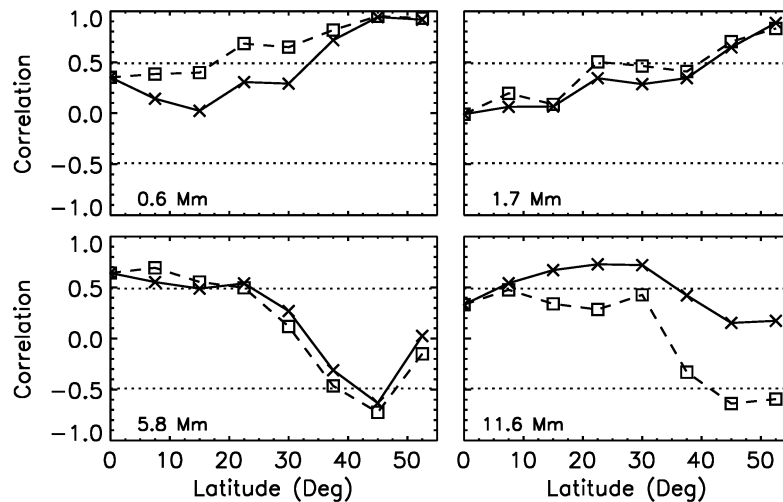


Figure 2. Linear correlation between meridional flow and  $B_0$ -angle variation at four depths for northern (solid line, crosses) and southern hemisphere (dashed line, squares). The dotted lines indicate the 99.9% significance levels.

four Carrington rotations out of phase with the  $B_0$ -angle. Since the apparent semi-diameter and the sidereal-synodic correction vary in phase, it is sufficient to use only one of them. We then repeat the correlation analysis for the zonal flow.

Figure 3 summarizes the results by showing the coefficients of a linear correlation between  $B_0$ -angle (top) and apparent semi-diameter variation (bottom) with the two horizontal-flow components. The correlation between meridional flow and  $B_0$ -angle shows a complex behavior with high positive values close to the surface at high latitudes, at depths between about four and ten Mm at latitudes equatorward of about  $20^\circ$ , and at greater depths in the northern hemisphere. In addition, there are regions of large anticorrelation at high latitudes at depths between about four and ten Mm. The temporal variation of the zonal flow is, by comparison, less correlated with the  $B_0$ -angle variation. It is significantly correlated with the  $B_0$ -angle only in the southern hemisphere at depths between two and 11 Mm. At the same depth range in the northern hemisphere, the correlation is negative and increases in amplitude with increasing latitude but remains below the 99.9% significance level. The correlations between the apparent semi-diameter and the zonal and meridional flow are much smaller compared to the ones with the  $B_0$ -angle.

Figure 4 shows the same as Figure 3 but for the errors of the horizontal flows. The errors of both flow components are clearly correlated with the temporal variation of the  $B_0$ -angle, with positive values in the southern and negative ones in the northern hemisphere. The correlation values increase with increasing latitude and the most equatorward latitudes with significant correlations occur at a depth of about five Mm. The flow errors show hardly any correlation with the apparent semi-diameter variation.

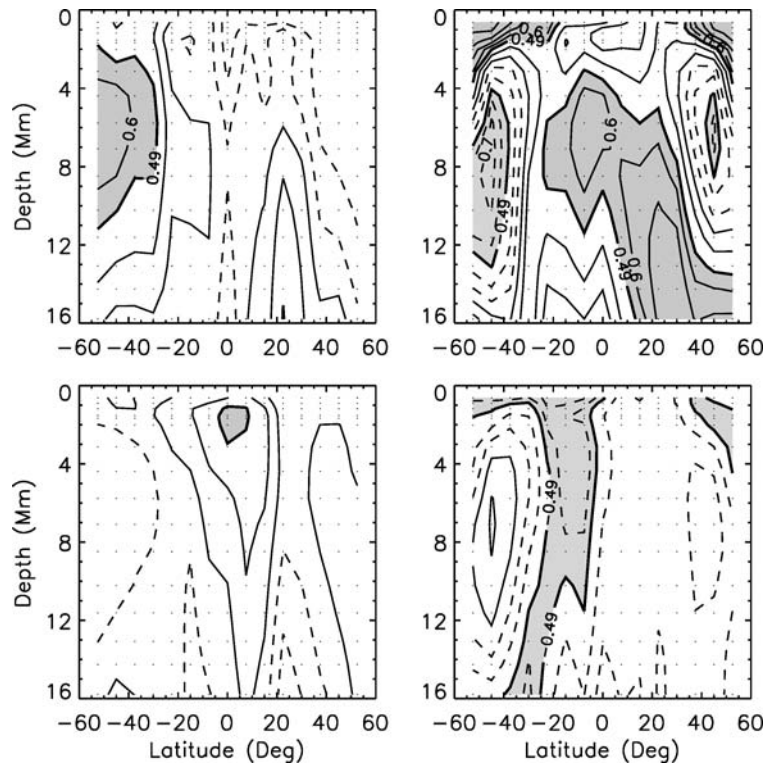


Figure 3. Coefficients of a linear correlation between  $B_0$ -angle and apparent semi-diameter variation with the two horizontal flow components as functions of latitude and depth: *Top-left*:  $B_0$ -angle and zonal flow; *top-right*:  $B_0$ -angle and meridional flow; *bottom-left*: semi-diameter and zonal flow; *bottom-right*: semi-diameter and meridional flow. The grey areas indicate values greater than the 99.9% significance level represented by thick solid contour lines (of 0.49). Solid (dashed) contour lines indicate positive (negative) correlations (0.1, 0.3, 0.6, 0.7, 0.8, 0.9). Dots indicate the depth-latitude grid of the ring-diagram analysis.

Figure 5 shows the temporal variation of the meridional flow after removing the  $B_0$ -angle effect by subtracting the fit of a linear regression between flow and  $B_0$ -angle variation. The one-year periodicity has disappeared. Consequently, one can conclude that such a periodicity is purely a systematic effect due to the  $B_0$ -angle. However, the “counter cell” still appears at high latitude in shallow layers in both hemispheres. While the meridional flow is nearly constant with time at many locations close to  $22.5^\circ$ , its amplitude noticeably increases with time at  $37.5^\circ$  latitude and decreases at  $7.5^\circ$  at depths of 1.7 and 5.8 Mm in both hemispheres. Fluctuations on time scales shorter than one year seem to be unrelated between the hemispheres.

Figure 6 shows the variation of the zonal flow. The tracking rate has been subtracted and the sidereal-synodic correction has been added. While the correlation between the zonal flow and the  $B_0$ -angle is not significant except at high latitudes at some depths in the southern hemisphere, it shows the same pattern with latitude

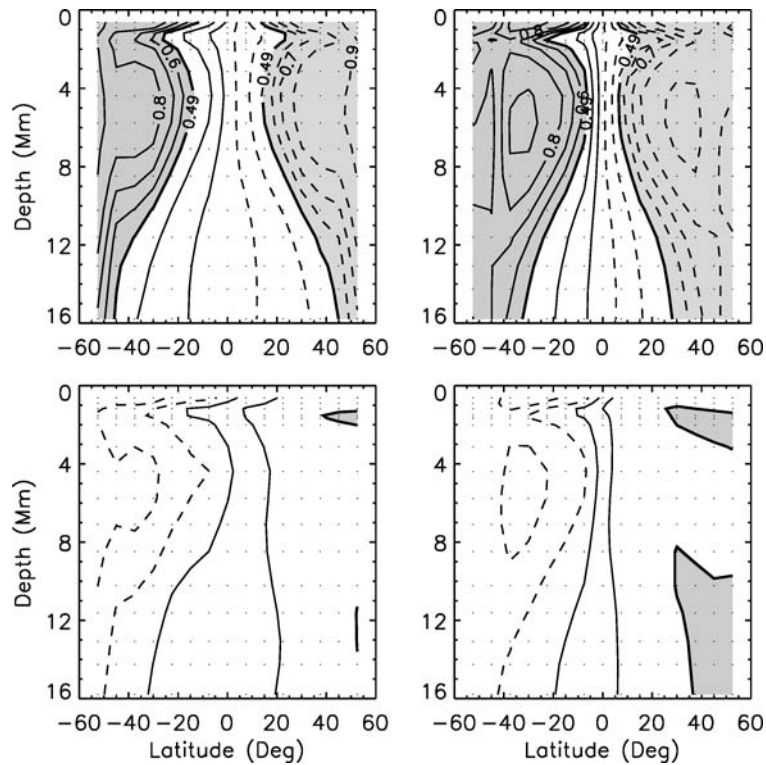


Figure 4. Same as Figure 3 for correlations with flow errors: *Top-left*:  $B_0$ -angle and zonal flow error; *top-right*:  $B_0$ -angle and meridional-flow error; *bottom-left*: semi-diameter and zonal flow error; *bottom-right*: semi-diameter and meridional-flow error.

and depth as the correlation between the errors of the zonal flow and the  $B_0$ -angle. For this reason, we decided to remove the  $B_0$ -angle effect from the zonal flow, as shown in Figure 6. The zonal flow values are generally larger in the southern than in the northern hemisphere, which is most apparent at high latitudes. The zonal flow shows strong fluctuations on time scales shorter than one year, which appear to be correlated between the hemispheres at  $7.5^\circ$  and  $22.5^\circ$  latitude. At latitudes poleward of about  $40^\circ$ , the variation of the zonal flow appears to have a larger amplitude compared to more equatorward latitudes.

To estimate the magnitude of these fluctuations, we calculate the rms value of the meridional flow and find an average value of  $3.1 \pm 0.6$  m/s over all latitudes and depths. The average rms value ( $3.0 \pm 1.0$  m/s) of the zonal flow is very close to this value, but the zonal-flow average is the result of a bowl-shaped variation with latitude with a value of  $2.3 \pm 0.3$  m/s averaged over latitudes equatorward of  $25^\circ$  and a value of  $4.2 \pm 0.7$  m/s averaged over latitudes poleward of  $40^\circ$ . At face value, this result implies that the zonal flows are “noisier” than meridional flows at high latitudes, while the opposite is true at low latitudes. These fluctuations are much larger than the average error of 0.5 m/s for zonal and meridional flow. Before

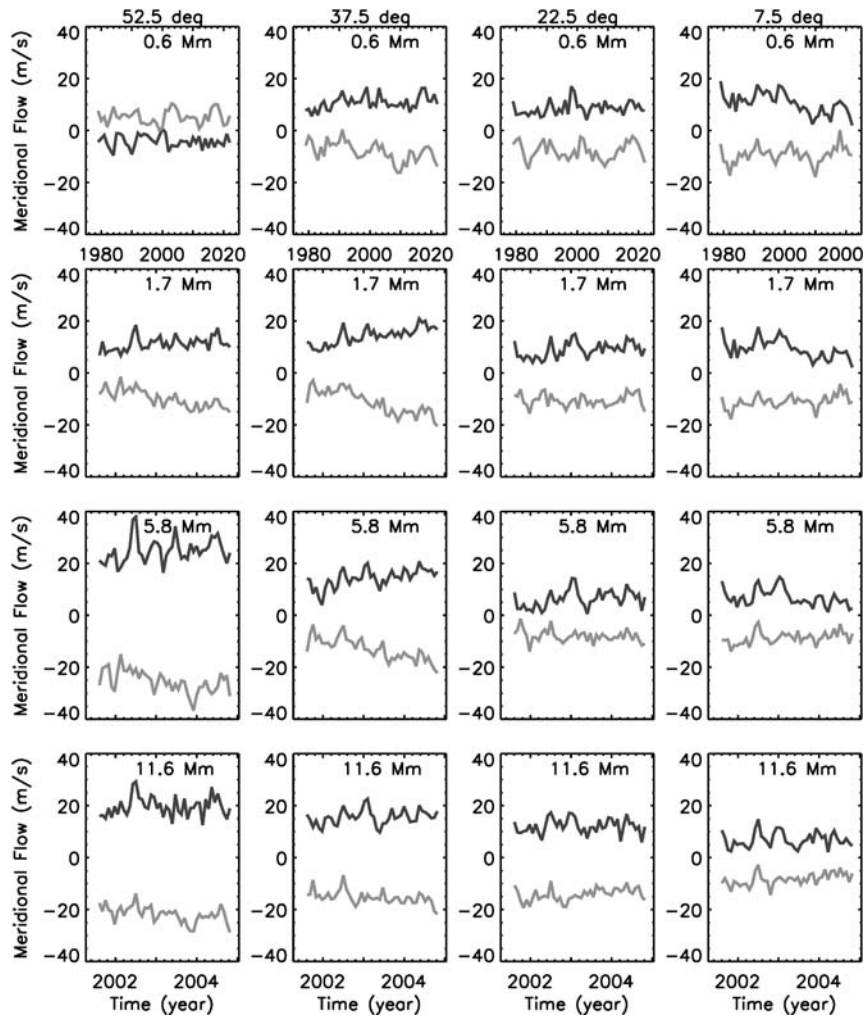


Figure 5. Same as Figure 1 after removing the  $B_0$ -angle variation from the meridional flow.

the  $B_0$ -angle corrections, the rms fluctuations of both zonal and meridional flow show a bowl-shaped variation with  $2.3 \pm 0.3$  m/s equatorward of  $25^\circ$  latitude and  $4.7 \pm 0.7$  m/s poleward of  $40^\circ$  latitude for the zonal flow and  $3.2 \pm 0.6$  m/s and  $5.0 \pm 1.4$  m/s for the meridional flow. As expected from the correlation results, the correction has the greatest effect at high latitudes.

### 3.2. NORTH-SOUTH COMPARISON

Figure 7 shows linear correlation coefficients between flows in the northern and southern hemisphere. While the short-term variations of the zonal flow are highly correlated at low latitudes, at latitudes poleward of  $45^\circ$ , the variations are

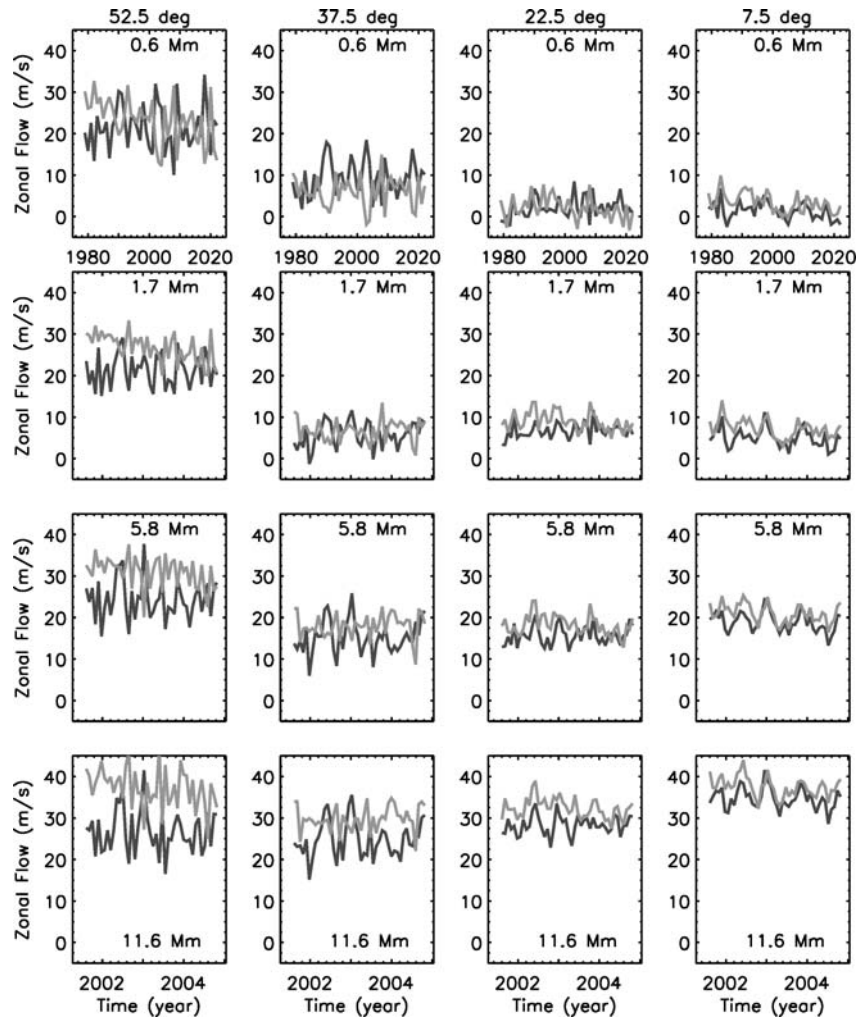


Figure 6. Temporal variation of the zonal flow in the northern (*dark grey*) and southern hemisphere (*light grey*) at four latitudes and four depths after removing the  $B_0$ -angle variation. The surface rotation rate (tracking rate) has been subtracted (Snodgrass, 1984) and the sidereal-synodic correction has been added. The *line thickness* represents about two standard deviations of the formal uncertainty. The top row shows, for comparison, the time scale in Carrington Rotations.

significantly anticorrelated between the hemispheres. The range of latitudes with significant correlations is greatest at a depth of about nine Mm. The correlation is close to zero at about  $30^\circ$ . While this correlation might be of solar origin, we cannot rule out that it is due to some other systematic effect. The meridional flow shows hardly any significant correlation between the temporal variation in the two hemispheres. The positive correlation values near  $30^\circ$  at about two Mm reflect the trends seen in Figure 5.

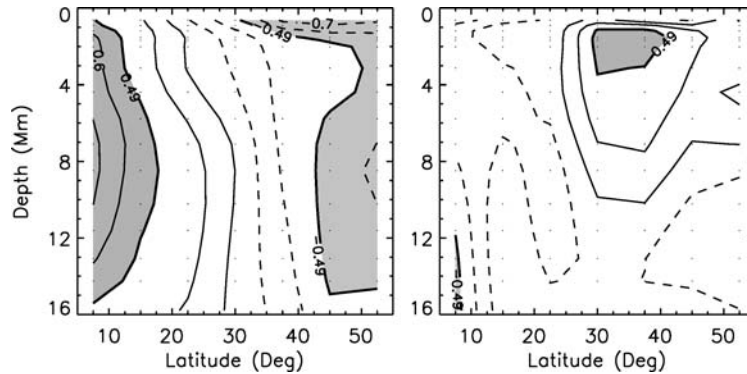


Figure 7. Linear correlations between flows in the northern and southern hemisphere as a function of latitude and depth for zonal (*left*) and meridional flow (*right*). The annual variations due to the  $B_0$ -angle have been removed. The grey areas indicate correlations greater than the 99.9% significance level represented by thick solid contour lines (of 0.49). Solid (*dashed*) contour lines indicate positive (negative) correlations (0.1, 0.3, 0.6, 0.7). The *dots* indicate the depth-latitude grid of the ring-diagram analysis.

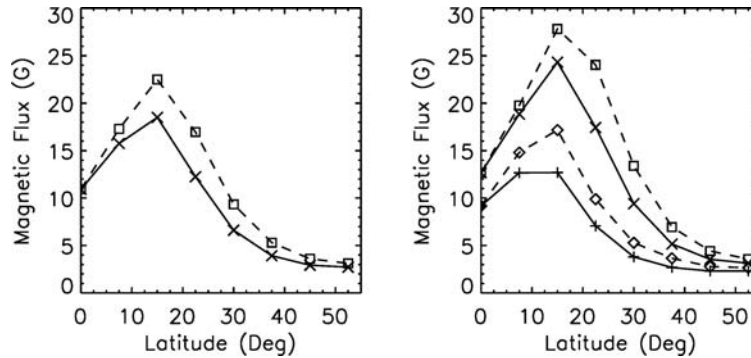


Figure 8. *Left*: Unsigned magnetic flux averaged over 44 Carrington rotations as a function of latitude for the northern (*solid, crosses*) and southern hemisphere (*dashed, squares*). *Right*: Unsigned magnetic flux averaged over two subsets of 22 Carrington rotations 1979–2000 (*crosses, squares*) and 2001–2022 (*plus signs, diamonds*) for the northern (*solid*) and southern hemisphere (*dashed*).

Since some variations might be related to the distribution of magnetic flux, Figure 8 shows average unsigned flux values as a function of latitude. The unsigned magnetic flux of CR 1979–2022 is on average larger in the southern hemisphere than in the northern one; the greatest differences occur at  $15^\circ$  and  $22.5^\circ$  latitude. To indicate the temporal variation of activity, we divide the data into two subsets of higher and lower average magnetic activity, which cover CR 1979–2000 (July 2001 to March 2003) and CR 2001–2022 (March 2003 to November 2004). The mean latitude of activity is at about  $15^\circ$  and moves from somewhat poleward of  $15^\circ$  during the high-activity subset to somewhat equatorward of  $15^\circ$  during the low-activity subset. The shift in mean-latitude position is about the same as the distance

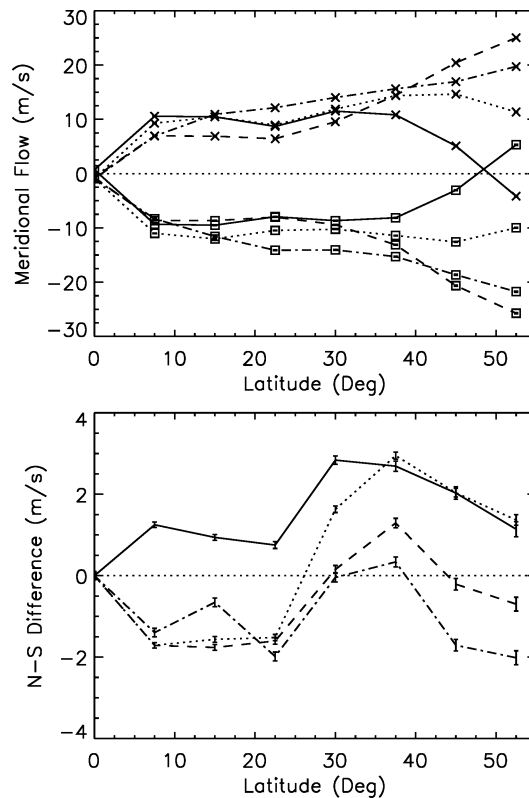
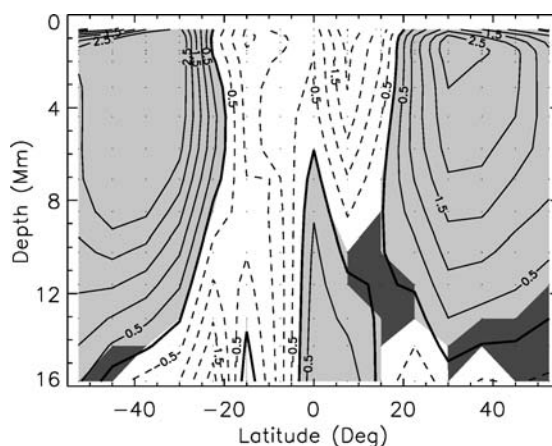


Figure 9. Top: Average meridional flow as a function of latitude at four different depths (0.6 Mm: solid, 1.7 Mm: dotted, 5.8 Mm: dashed, 11.6 Mm: dot-dashed) for the northern (crosses) and the southern hemisphere (squares). Positive (negative) values indicate flows to the North (South). Bottom: Difference between the meridional flow derived in the northern and southern hemispheres. Positive (negative) values imply greater poleward flow in the northern (southern) hemisphere.

between two dense-pack grid points. The unsigned magnetic flux decreases with time at all latitudes during the period of the observations, which coincides with an increase in the meridional flow at latitudes greater than  $30^\circ$  at most depths (Figure 5) and a decrease in the zonal flow at  $52.5^\circ$  in the southern hemisphere (Figure 6).

Next, we calculate the meridional flow averaged over CR 1979 – 2022 corrected for the  $B_0$ -angle variation. The top panel of Figure 9 shows the average flow as a function of latitude at four different depths. The meridional flows in both hemispheres show steep gradients at latitudes of about  $35^\circ$  or  $40^\circ$  and higher. At these latitudes, the flow amplitudes decrease with increasing latitude at shallow depths (below about two Mm), while they increase with latitude at greater depths and then decrease again at depths greater than about 13 Mm (not shown). The counter cell is noticeable close to the surface at the highest latitudes. The bottom panel of Figure 9 shows that the poleward meridional flow has a larger amplitude in the southern



*Figure 10.* The slope of a linear regression with time of the meridional flow in units of m/s per year. The sign of the flow has been changed in the southern hemisphere so that positive (negative) values imply an increase (decrease) in flow amplitude in either hemisphere. The dots indicate the depth-latitude grid. Solid (dashed) contours indicate positive (negative) slopes with a spacing of 0.5 m/s. Dark grey areas indicate locations where the slope is less than three times its error; light grey areas highlight positive values.

hemisphere for almost all depths at latitudes equatorward of  $25^\circ$ , except close to the surface. At mid-latitudes between  $25^\circ$  and  $40^\circ$ , the meridional flow is larger in the northern hemisphere. The latitudes with the largest excess poleward flow in the southern hemisphere ( $10^\circ$  to  $25^\circ$ ) coincide with the latitudes of the largest excess magnetic flux in the southern hemisphere. At latitudes poleward of  $40^\circ$ , the meridional flow is stronger in the northern hemisphere at shallower depths and larger in the southern one at greater depth.

We now revisit the long-term variation of the meridional flow and represent it with a linear regression with time. Figure 10 shows the resulting slope as a function of depth and latitude. The mean location of magnetic activity appears to be a dividing line. Near the mean latitude of activity and equatorward of it, the slope is generally negative implying that the flow amplitude is larger during high magnetic activity and decreases during the declining phase of the cycle. Exceptions are the deeper layers in the northern hemisphere. On the poleward side of magnetic activity, the slope is generally positive which indicates that the meridional flow amplitude increases with decreasing activity. Exceptions are the deepest layers especially in the northern hemisphere and the near-surface layers at  $0.6$  Mm at  $52.5^\circ$  latitude. The positive slopes are generally larger in the southern hemisphere than in the northern one.

The average zonal flow corrected for the  $B_0$  angle variation is shown in Figure 11 as a function of latitude at four depths. The zonal flow increases in amplitude with increasing depth, as expected from measurements of the rotation rate (e.g., Howe *et al.*, 2006). The amplitude shows a local maximum near  $15^\circ$  latitude or less, which

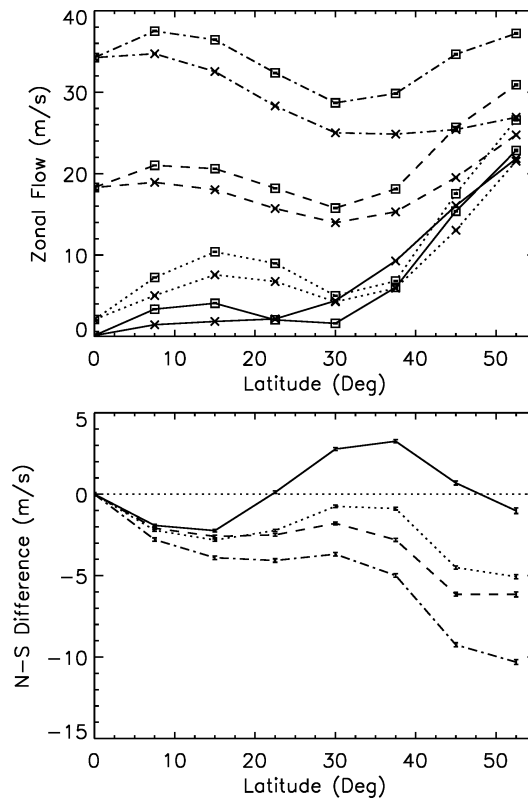


Figure 11. Same as Figure 9 for the average zonal flow. In the *bottom panel*, positive (negative) values imply greater zonal flow in the northern (southern) hemisphere.

coincides with the mean latitude of magnetic flux, and a local minimum near  $30^\circ$ . This latitudinal variation is most likely a consequence of the solar-cycle variation of the zonal flow, the torsional-oscillation pattern. The zonal flow is predominantly faster in the southern hemisphere than in the northern one. The differences generally increase with increasing latitude for latitudes greater than  $25^\circ$ . Furthermore, the difference in amplitude between the hemispheres increases with depth with a local maximum near  $15^\circ$  latitude. The high- and low-activity subsets of CR 1979–2000 and CR 2001–2022 show essentially the same behavior (not shown). The most obvious difference is that the local maximum is clearly at  $15^\circ$  for CR 2001–2022 and closer to  $22.5^\circ$  for CR 1979–2000, following the change in mean latitude of activity from higher to lower latitude.

The North–South asymmetry of the zonal flow appears to consist of one component that relates to the distribution of magnetic activity (at latitudes less than  $30^\circ$ ) and another one that describes a general increase in asymmetry with latitude. To quantify the second component, we calculate a linear fit with latitude of the North–South difference of the average zonal flow (CR 1979–2022). Figure 12 shows the

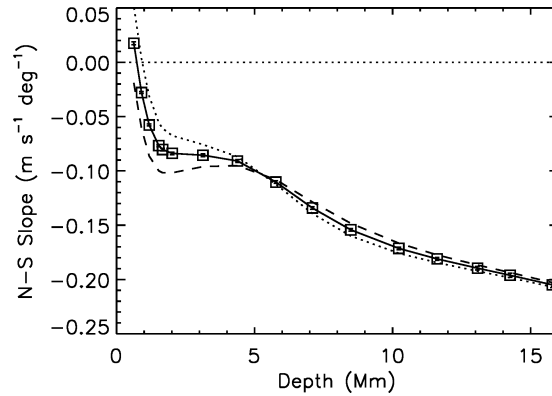


Figure 12. Slope of a linear regression with latitude of the North–South difference of the zonal flow as a function of depth for CR 1979–2022 (solid line, squares), CR 1979–2000 (dashed line), and for CR 2001–2022 (dotted line).

resulting slope as a function of depth. The slope is negative at all depths implying faster zonal flows in the southern hemisphere than in the northern one, except near the surface where there is almost no North–South asymmetry. The magnitude of the slope increases with depth; about half of the increase occurs in the outer two Mm and the asymmetry barely changes between two and five Mm. The two subsets of CR 1979–2000 and CR 2001–2022 show the same behavior, as expected from the previous paragraph. However, at depths less than about five Mm, the North–South asymmetry of the subset with less magnetic activity (CR 2001–2022) is smaller than the one with higher activity (CR 1979–2000). This is mainly due to a decrease in zonal flow amplitude in the southern hemisphere at high latitudes (noticeable in Figure 6). At greater depth both subsets lead to similar slopes.

#### 4. Summary and Discussion

We have analyzed 44 consecutive Carrington rotations and explored the horizontal flow components, their temporal variation and their North–South asymmetry. The meridional flow shows an annual variation related to the  $B_0$ -angle, as noticed by González Hernández *et al.* (2006). The flow errors also vary in time with the variation of the  $B_0$ -angle. Komm *et al.* (2005) found that the velocity errors show a bowl-shaped dependence with latitude most likely due to geometric foreshortening. It is thus not too surprising that the errors show an annual variation in phase with the  $B_0$ -angle, since a non-zero  $B_0$ -angle will either enhance or diminish the foreshortening at a given solar latitude. Furthermore, since this variation affects the spatial resolution in the North–South direction, this can explain why the meridional flow would also show such a variation, while the zonal flow, a flow in the East–West

direction, would be less affected by such a variation. The  $B_0$ -angle variation affects flows differently at different layers for a given latitude. This implies that its effect on the observations varies with spatial wavenumber. It is somewhat surprising that the  $B_0$ -angle effect can be different between the hemispheres. One reason might be that different mode sets might be fitted in different dense packs and the inversions are performed on mode sets specific to each dense pack and not on the subset of common modes. To correct the horizontal flows for these annual variations, we subtract a linear regression in  $B_0$ -angle from the flows.

The meridional flow is generally poleward except near the surface at the highest latitudes where the flow is equatorward. This “counter cell” is present in both hemispheres at all times even after correcting for the  $B_0$ -angle effect. The existence of a counter cell at high latitudes in the meridional flow has been reported by Haber *et al.* (2002) analyzing MDI Dynamics Program data. However, the counter cell found in MDI data with a ring-diagram analysis is located at depths greater than about six Mm in the northern hemisphere. González Hernández *et al.* (2006) studied meridional flows with a large-aperture ring analysis of GONG++ data at depths about 60% deeper than those accessible with a standard ring-diagram analysis. They found that a counter cell appears at great depths during times of maximum  $B_0$ -angle and that it appears either in the northern or southern hemisphere depending on the sign of the  $B_0$ -angle. With counter cells unique to each data set or analysis method, we cannot rule out that the near-surface counter cell reported here is due to some systematic effect.

The average meridional flow has a larger amplitude in the southern hemisphere equatorward of the mean latitude of magnetic activity and a larger amplitude in the northern hemisphere poleward of the mean latitude. This is a consequence of a meridional flow that is composed of a poleward average component and a secondary one that converges toward the mean latitude of activity, as found in previous studies (*e.g.*, Haber *et al.*, 2002; Zhao and Kosovichev, 2004; Komm *et al.*, 2005), and a North–South asymmetry in magnetic flux with more activity in the southern hemisphere. The average meridional flow amplitude has a large gradient with depth at latitudes poleward of  $40^\circ$  compared to its variation with depth at lower latitudes. The amplitude of the meridional flow increases with decreasing magnetic activity at latitudes greater than about  $25^\circ$  which is poleward of the mean latitude of activity. This agrees with the variation at high latitudes observed by Basu and Antia (2003). At more equatorward latitudes, the meridional flow amplitude is larger during the epoch of high activity, which is a consequence of the convergence toward the mean latitude of activity. This “steepening” with increasing activity has been found by Haber *et al.* (2002) and by Zhao and Kosovichev (2004) in their analyses of MDI Dynamics Program data and this result also agrees with Chou and Ladenkov (2005) who found in deeper layers that the amplitude of the divergent flow correlates with the sunspot number variation.

The amplitude of the zonal flow is usually larger in the southern hemisphere than in the northern one during these 44 Carrington rotations except in the layers close

to the surface. This leads to a North–South asymmetry of the average flow that is close to zero near the surface and increases with depth, similar to the one derived from one year of GONG++ data by Komm *et al.* (2005). The current results show that the North–South asymmetry at depths less than about five Mm decreases with decreasing activity during the declining phase of the solar cycle. Basu and Antia (2003) found a similar North–South asymmetry in the zonal flow derived from MDI data and there are hints of a similar solar-cycle variation in their work.

The meridional and zonal flow patterns and their North–South asymmetry are strongly related to the distribution of magnetic activity and hence to the solar cycle. The GONG++ data set used here is the longest consecutive data set available for local helioseismology, but it still covers only about 30% of an 11-year cycle. The systematic variations of non-solar origin show the importance of continuous coverage, which will be possible with the Helioseismic and Magnetic Imager instrument onboard the Solar Dynamics Observatory and the on-going operation of GONG.

### Acknowledgements

This work was supported by NASA grant NNG 05HL41. This work utilizes data obtained by the Global Oscillation Network Group (GONG) program, managed by the National Solar Observatory, which is operated by the Association of Universities for Research in Astronomy (AURA), Inc. under a cooperative agreement with the National Science Foundation. The data were acquired by instruments operated by the Big Bear Solar Observatory, High Altitude Observatory, Learmonth Solar Observatory, Udaipur Solar Observatory, Instituto de Astrofísica de Canarias, and Cerro Tololo Interamerican Observatory. NSO/Kitt Peak data used here are produced cooperatively by NSF/NSO, NASA/GSFC, and NOAA/SEC. SOLIS VSM data used here are produced cooperatively by NSF/NSO and NASA/GSFC. The ring-fitting analysis is based on algorithms developed by Haber, Hindman, and Larsen with support from NASA and Stanford University. We thank the referee for helpful comments.

### References

- Basu, S. and Antia, H.M.: 2003, *Astrophys. J.* **585**, 553.  
Charbonneau, P.: 2005, *Living Rev. Solar Phys.* **2**, No. 2  
(<http://solarphysics.livingreviews.org/lrsp-2005-2>).  
Chou D.-Y. and Dai, D.-C.: 2001, *Astrophys. J.* **559**, L175.  
Chou D.-Y. and Ladenkov, O.: 2005, *Astrophys. J.* **630**, 1206.  
Corbard, T., Toner, C., Hill, F., Hanna, K.D., Haber, D.A., Hindman, B.W., and Bogart, R.S.: 2003, in H. Sawaya-Lacoste (ed.), *Local and Global Helioseismology: The Present and Future*, (ESA SP-517), ESA, Noordwijk, Netherlands, p. 255.  
Dikpati, M. and Gilman, P.: 2001, *Astrophys. J.* **559**, 428.  
Dikpati, M., de Toma, G., Gilman, P.A., Arge, C.N., and White, O.R.: 2004, *Astrophys. J.* **601**, 1136.

- González Hernández, I., Komm, R., Hill, F., Howe, R., Corbard, T., and Haber, D.A.: 2006, *Astrophys. J.* **638**, 576.
- Gough, D.O. and Toomre, J.: 1983, *Solar Phys.* **82**, 401.
- Haber, D.A., Hindman, B.W., Toomre, J., Bogart, R.S., Larsen, R.M., and Hill, F.: 2002, *Astrophys. J.* **570**, 885.
- Harvey, J., Tucker, R., and Britanik, L.: 1998, in S.G. Korzennik and A. Wilson (eds.), *Structure and Dynamics of the Interior of the Sun and Sun-like Stars*, (ESA SP-418), ESA, Noordwijk, Netherlands, p. 209.
- Hill, F.: 1988 *Astrophys. J.* **339**, 996.
- Hill, F., Bolding, J., Toner, C., Corbard, T., Wampler, S., Goodrich, B., Goodrich, J., Eliason, P., and Hanna, K.D.: 2003, in H. Sawaya-Lacoste (ed.), *Local and Global Helioseismology: The Present and Future*, (ESA SP-517), ESA, Noordwijk, Netherlands, p. 295.
- Howe R., Komm, R., Hill, F., Ulrich, R., Haber, D.A., Hindman, B.W., Schou, J., and Thompson, M.J.: 2006, *Solar Phys.* **235**, 1.
- Komm, R., Howe R., Hill, F., González-Hernández, I., Toner, C., and Corbard, T.: 2005, *Astrophys. J.* **631**, 636.
- Morrow, C.A.: 1988, Ph.D. Thesis U. Colorado and NCAR, NCAR Coop. Thesis No. 116.
- Nandy, D. and Choudhuri, A.R.: 2002, *Science* **296**, 1671.
- Snodgrass, H.B.: 1984, *Solar Phys.* **94**, 13.
- Thompson, M.J., *et al.*: 1996, *Science* **272**, 1300.
- Toner, C., Haber, D.A., Corbard, T., Bogart, R.S., and Hindman, B.W.: 2003, in H. Sawaya-Lacoste (ed.), *Local and Global Helioseismology: The Present and Future*, (ESA SP-517), ESA, Noordwijk, Netherlands, p. 405.
- Wittmann, A.D., *et al.*: 1996, *Solar Phys.* **168**, 211.
- Zhao, J. and Kosovichev, A.G.: 2004, *Astrophys. J.* **603**, 776.